Receiver Functions of Seismic Waves in Layered Anisotropic Media: Application to the Estimate of Seismic Anisotropy

by Mamoru Nagaya, Hitoshi Oda, Hirokazu Akazawa, and Motoko Ishise

Abstract   We investigate the effect of seismic anisotropy on *P*-wave receiver functions, calculating synthetic seismograms for *P*-wave incidence on multilayered anisotropic structure with hexagonal symmetry. The main characteristics of the receiver functions affected by the anisotropy are summarized as (1) appearance of seismic energy on radial and transverse receiver functions, (2) systematic change of *P*-to-*S* (*Ps*) converted waveforms on receiver functions as ray back-azimuth increases, and (3) reversal of the *Ps*-phase polarity on the radial receiver function in a range of the back azimuth. Another important influence is shear-wave splitting of the *Ps*-converted waves and other later phases reverberated as *S* wave. By numerical experiments using synthetic receiver functions, we demonstrate that the waveform cross-correlation analysis is applicable to splitting *Ps* phases on receiver functions to estimate the seismic anisotropy of layer structure. Advantages to utilizing the *Ps* phases are (1) they appear more clearly on receiver functions than on seismograms and (2) they inform us about what place along the seismic ray path is anisotropic. Real analysis of shear-wave splitting is executed to the Moho-generated *Ps* phases that are identified on receiver functions at six seismic stations in the Chugoku district, southwest Japan. The time lags between the two arrivals of the split *Ps* phases are estimated at 0.2–0.7 sec, and the polarization directions of the fast arrival components are from north–south to northeast–southwest. This result is consistent with recent results of shear-wave splitting measurements and the trend of linear epicenter distributions of crustal earthquakes and active fault strikes in the Chugoku district.

Introduction

The observations of shear-wave splitting have been widely performed to detect seismic anisotropy in the crust and mantle (e.g., Ando, 1984; Fukao, 1984; Silver and Chang; 1988; Kaneshima, 1990). The shear-wave splitting is effective to diagnose that seismic anisotropy resides somewhere on a propagation path of shear wave, but it has the inherent shortcoming that the depth resolution is poor to find what zone on the ray path is anisotropic. If antecedents of seismic waves that we are going to analyze are exactly known, such as the *Ps* phase generated by *P*-to-*S* conversion at a velocity discontinuity, the shortcoming would be circumvented. Thus, we intend to utilize the *Ps*-converted waves to estimate the anisotropic velocity structure in the crust and upper mantle. The *Ps* phase travels as a shear wave after the *P*-to-*S* conversion at the velocity discontinuity, so it is thought to have the characteristic of shear-wave splitting because of shear-wave polarization anisotropy that is caused by seismic anisotropy in layers above the discontinuity, that is, the *Ps* wave splits into two components that propagate with different velocities. If the polarization anisotropy of the *Ps* phase is detected by shear-wave splitting analysis, it provides

us with information about the seismic anisotropy in layers overlying the discontinuity; consequently, we know what place along the seismic ray path is anisotropic. However, clear *Ps*-converted waves to which the shear-wave splitting analysis is applicable are rarely recorded on observed seismograms from local earthquakes because of complexities of source time functions and contaminations of noise and other seismic phases.

We think that the *P*-wave receiver function can be utilized to identify clear *Ps*-converted waves, because the source time function is eliminated from it. The receiver function method has been developed to find velocity discontinuities beneath various regions and to estimate their three-dimensional configurations (e.g., Langston, 1979; Owens *et al.*, 1984; Shibutani *et al.*, 1996; Peng and Humphreys, 1998; Zhu and Kanamori, 2000; Yamauchi *et al.*, 2003). The method is excellent at clearly showing the *Ps* phases on the receiver functions even if seismograms are contaminated by noise and scattering waves. Thus, we intend to execute shear-wave splitting analysis to the *Ps* phases on receiver functions. The first attempt to measure the shear-wave

splitting of the *Ps* phase was made by McNamara and Owens (1993). Further, how the seismic anisotropy influences the *Ps* phases on receiver functions was theoretically and observationally examined by subsequent studies (e.g., Levin and Park, 1997, 1998; Peng and Humphreys, 1997; Savage, 1998). These studies showed that the polarization anisotropy was detectable by the splitting analysis of the *Ps* phases on the receiver functions. In this study, we review the effect of seismic anisotropy on the *Ps* phases, calculating synthetic receiver functions for layered structures of isotropic and anisotropic velocities, and we address some issues on the splitting analysis of the *Ps* phases.

The splitting analysis is really carried out to *Ps*-converted waves on *P*-wave receiver functions obtained from teleseismic waveform data at seismic stations in the Chugoku district, southwest Japan. What we measure by the analysis is the fast polarization direction of two components of splitting *Ps* phase and the time lag between two arrivals of the split *Ps* phase. It is well known in the crust that the fast polarization directions of direct *S* waves are nearly parallel to trajectories of maximum principal stress acting on the Japan Islands (Kaneshima, 1990). The crustal anisotropy is interpreted as being due to crack-induced anisotropy, which is caused by the alignment of open cracks produced by the maximum principal stress (Crampin, 1981). In the Chugoku district, the direction of maximum principal stress is known to be in a nearly northwest–southeast direction (Ando, 1979; Tsukahara and Kobayashi, 1991). Thus, the fast polarization direction of the shear wave is expected to be in the same direction as the maximum principal stress. But Iidaka (2003) reported by the splitting analysis of two phases reverberated in the crust that the fast polarization directions were inconsistent with the maximum principal stress direction in southwest Japan. This result may arise because the seismic phases analyzed in Iidaka's study were not clear enough to apply the splitting analysis. Recently, high-quality seismic waveform data from the *F*-net, which is a broadband seismic network deployed over Japan, were analyzed for study of seismic anisotropy in the upper mantle under the Japan Islands (e.g., Long and van der Hilst, 2005, 2006). In this article, after calculating *P*-wave receiver functions from the seismic records at the *F*-net stations and temporal stations in the Chugoku district, we find clear *Ps* phases converted at the Moho discontinuity. The fast polarization direction and the delay times are estimated by the splitting analysis of the *Ps* phases on the receiver functions. In addition, we investigate regional variation of the seismic anisotropy within the crust and examine the relationship between lateral variation of the fast polarization direction and tectonic stress acting on southwest Japan.

Description of Anisotropic Structure and Calculation Method of Receiver Functions

The study of seismic-wave propagation in layered anisotropic structure was started by Crampin (1970); subsequent studies were done for complicated velocity structures includ-

ing seismic anisotropy and dipping velocity discontinuity (e.g., Keith and Crampin, 1977a,b; Levin and Park, 1977; Fryer and Frazer, 1984; Savage, 1998, Frederiksen and Bostock, 2000). In this section, we explain the parameters used to describe anisotropic velocity structure and briefly present how to calculate synthetic seismograms and receiver functions of seismic body waves propagating into a stratified anisotropic medium.

Olivine and enstatite crystals, the major anisotropic minerals in peridotite (which is considered to be a candidate of upper mantle material), possess orthorhombic symmetry (Anderson, 1989), but the elastic behavior of typical peridotite samples is well approximated by hexagonal symmetry (Montagner and Anderson, 1989; Mainprice and Silver, 1993). Hexagonal symmetry is also appropriate for the elastic property of the medium containing aligned cracks, such as the upper crust (Crampin, 1978; Hudson, 1981; Kaneshima, 1991). Therefore, the upper mantle and the crust are assumed to have seismic anisotropy of hexagonal symmetry. The seismic velocity perturbations arising from weak hexagonal anisotropy are written as (Backus 1965; Park and Yu 1992)

$$(\alpha^2 - \alpha_0^2)/\alpha_0^2 = A + B\cos 2\eta + C\cos 4\eta; \quad \text{for } P \text{ wave}$$
$$(\beta^2 - \beta_0^2)/\beta_0^2 = D + E\cos 2\eta; \quad \text{for } S \text{ wave}, \tag{1}$$

where α and β are the *P*- and *S*-wave velocities, respectively, and η is the angle between the hexagonal-symmetry axis and the propagation direction of the seismic wave. Parameters with subscript 0 denote the isotropic velocities of *P* and *S* waves. Dimensionless parameters (B, C, and E) denote the anisotropic velocity perturbations, and A and D are the isotropic velocity perturbations. When the *c* axis in Cartesian coordinates of $(a, b, c) \equiv (1, 2, 3)$ is taken as the hexagonal-symmetry axis, the elastic constants C_{ijkl} are written as follows (Park and Yu, 1992):

$$C_{1111} = C_{2222} = (1 + A - B + C)\rho\alpha_0^2,$$
$$C_{3333} = (1 + A + B + C)\rho\alpha_0^2,$$
$$C_{1122} = (1 + A - B + C)\rho\alpha_0^2 - 2(1 + D - E)\rho\beta_0^2,$$
$$C_{1133} = C_{2233} = (1 + A - 3C)\rho\alpha_0^2 - 2(1 + D + E)\rho\beta_0^2,$$
$$C_{1313} = C_{2323} = (1 + A + B + C)\rho\beta_0^2,$$
$$C_{1212} = (C_{1111} - C_{1122})/2, \tag{2}$$

where ρ is the density. Further, the elastic constants satisfy the relationship of

$$C_{ijkl} = C_{jikl} = C_{ijlk} = C_{klij}. \tag{3}$$

The elastic constants other than those specified by equations (2) and (3) are equal to zero. Another Cartesian coordinate system of $(x_1, x_2, x_3) \equiv (1', 2', 3')$ is set in a semi-infinite layered medium, where the ground surface is the $x_1 - x_2$ plane and the x_3 axis is taken vertically downward

to the ground surface. The elastic constants C_{ijkl} are transformed into those $c_{i'j'k'l'}$ defined in the (x_1, x_2, x_3) coordinate system through

$$c_{i'j'k'l'} = U_{ii'} U_{jj'} U_{kk'} U_{ll'} C_{ijkl}. \quad (4)$$

The matrix elements $U_{ii'}$ are given by

$$\mathbf{U} = \begin{pmatrix} \cos\xi\cos\lambda & \cos\xi\sin\lambda & -\sin\xi \\ -\sin\lambda & \cos\lambda & 0 \\ \sin\xi\cos\lambda & \sin\xi\sin\lambda & \cos\xi \end{pmatrix}, \quad (5)$$

where ξ is the tilt angle of the hexagonal-symmetry axis measured from the x_3 axis; λ is the azimuth of the symmetry axis measured clockwise from the north (x_1 axis). Thus, the elastic constants $c_{i'j'k'l'}$ are calculated by using equation (4) if we specify the dimensionless parameters (A, B, C, D, E) of isotropic and anisotropic velocity perturbations, the orientation of hexagonal-symmetry axis (ξ, λ), the isotropic velocities of P and S waves (α_0, β_0), and the density ρ.

Synthetic seismograms of seismic waves traveling through a horizontally layered structure are calculated by using the equation

$$u_i(t) = h_i(t) * s(t), \quad (6)$$

where $u_i(t)$ and $h_i(t)$ are the ith components of the displacement vector and transfer functions, respectively, $s(t)$ denotes the earthquake source time function, and the symbol $*$ represents the convolution operator. The layer matrix method of Crampin (1970) is employed to calculate the transfer functions $h_i(t)$ of the layered anisotropic structure, each layer of which is specified by eleven parameters $(\alpha_0, \beta_0, \rho, A, B, C, D, E, \xi, \lambda)$ and layer thickness d. Radial and transverse receiver functions are defined for two pairs of radial and vertical component seismograms and of transverse and vertical component seismograms, respectively. According to Langston (1979), Fourier transform of the receiver function $r_i(t)$ is written as

$$R_i(\omega) = \frac{U_i(\omega)\bar{U}_Z(\omega)}{\Phi(\omega)} e^{-\omega^2/4a^2}, \quad (7)$$

where ω is the angular frequency, $U_i(\omega)$ denotes Fourier transform of $u_i(t)$, $\bar{U}_z(\omega)$ represents the complex conjugate of $U_z(\omega)$, a is the parameter to control the width of the Gaussian filter, and

$$\Phi(\omega) = \max\{U_z(\omega)\bar{U}_z(\omega), c\max[U_z(\omega)\bar{U}_z(\omega)]\}. \quad (8)$$

Here c denotes the water level. The receiver functions $r_i(t)$ in the time domain are obtained by calculating the inverse Fourier transform of $R_i(\omega)$, and their radial and transverse components are specified by replacing the subscript i with R and T, respectively.

The Effect of Seismic Anisotropy on Receiver Functions

We calculate synthetic seismograms and receiver functions for several models of layered anisotropic structure, assuming that a plane P wave is incoming from the isotropic bottom layer to the anisotropic structure. The incident angle is set at 10° measured from the vertical. One cycle sinusoidal wave with a period of 2 sec is assumed for the incident P wave. The values of the layer parameters $(\alpha_0, \beta_0, \rho, d, A, B, C, D, E, \xi, \lambda)$ of the velocity models are listed in Tables 1, 2, and 3. We set $C = 0$ in the models because the $\cos 4\eta$ term in equation (1) may be negligibly small in the upper mantle and crust (e.g., Park and Yu, 1992; Ishise and Oda, 2005, 2008). Figure 1a depicts synthetic seismograms calculated for a two-layered anisotropic structure (Model 1a) that consists of a 35 km thick anisotropic surface layer and isotropic bottom layer (Table 1). In the anisotropic surface layer, the symmetry axis lies horizontally in a north–south direction. Ray back azimuth of the incident wave is set at 45°, measured clockwise from the north. Because of the elasticity of hexagonal symmetry, both the radial and transverse components are excited. For comparison, synthetic

Table 1
Parameter Values of Model 1

Layer Number	α_0 (km/sec)	β_0 (km/sec)	ρ (g/cm³)	d (km)	B	E	Model 1a λ (°)	Model 1a ξ (°)	Model 1b λ (°)	Model 1b ξ (°)
1	6.7	3.8	2.7	35.0	0.02	0.04	0.0	90.0	0.0	45.0
2	7.8	4.5	3.3	0.0	0.00	0.00	—	—	—	—

Table 2
Parameter Values of Model 2

Layer Number	α_0 (km/sec)	β_0 (km/sec)	ρ (g/cm³)	d (km)	B	E	Model 2a λ (°)	Model 2a ξ (°)	Model 2b λ (°)	Model 2b ξ (°)
1	5.8	3.6	2.8	35.0	—	—	—	—	—	—
2	7.2	4.0	3.2	35.0	0.02	0.04	0.0	90.0	0.0	45.0
3	8.0	4.3	3.6	0.0	0.00	—	—	—	—	—

Table 3

Parameter Values of Model 3

Layer Number	α_0 (km/sec)	β_0 (km/sec)	ρ (g/cm^3)	d (km	B	E	$\lambda(°)$	ξ (°)
1	5.8	3.6	2.8	35.0	0.02	0.04	40.0	60.0
2	7.2	4.0	3.2	35.0	0.02	0.04	150.0	70.0
3	8.0	4.3	3.6	0.0	0.00	0.00	—	—
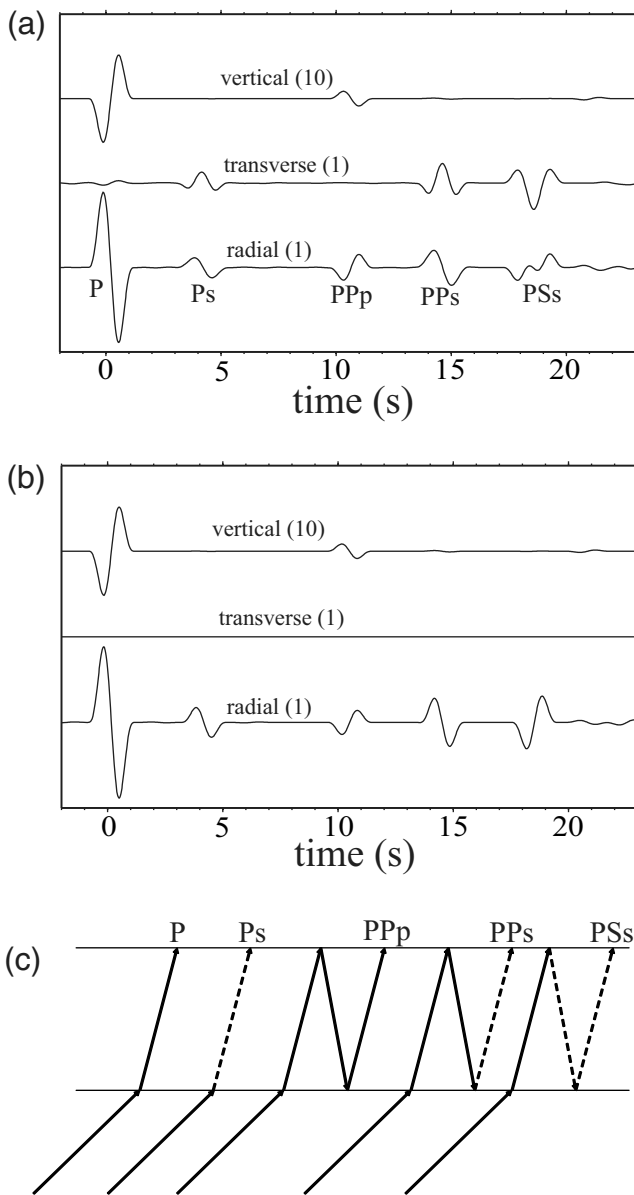
Figure 1. Synthetic seismograms for *P*-wave incidence: (a) anisotropic case (Model 1a) and (b) isotropic case ($B = 0$, $C = 0$, and $E = 0$). Numbers in parentheses denote scale factor of amplitude. (c) Ray paths of *Ps*-converted wave and reverberated waves in the surface layer. Solid and dashed lines represent the ray paths of *P* and *S* waves, respectively.

seismograms in an isotropic case ($B = 0$, $C = 0$, and $E = 0$) are represented in Figure 1b. The transverse component disappears, and the radial component agrees exactly with that calculated by the Thomson–Haskell layer matrix method (Haskell, 1962). In the anisotropic case (Fig. 1a), the first arrival phase is a direct *P* wave, the second phase is identified as a *Ps* phase generated by *P*-to-*S* conversion at the velocity discontinuity between the surface and bottom layers, and other later phases are *P* and *S* waves reverberated within the surface layer. The ray paths of these seismic phases are shown in Figure 1c. The waveform of the *Ps* phase on the transverse component is approximately proportional to the time derivative of that of the radial component, indicating that shear-wave splitting happens to the *Ps* phase during the propagation in the surface anisotropic layer (Silver and Chang, 1991). Similar splitting is also seen in waveforms of the later phases reverberated in the surface layer. These waveform characteristics are basically consistent with those pointed out by Levin and Park (1997).

We calculate radial and transverse receiver functions using three-component synthetic seismograms for several models of layered anisotropic structure. We set $c = 0.01$ and $a = 2.0$ in equations (5) and (7) for calculation of the receiver functions. The receiver functions for Model 1a are pasted up in the order of increasing ray back azimuth (see Fig. 2). *Ps*-converted phases are clearly identified at about 4 sec after initial *P* arrival time on the radial and transverse receiver functions. The *Ps*-phase waveform on the transverse receiver function is similar to the time derivative of that on a radial receiver function. This result means that shear-wave splitting happens to the *Ps* phase on receiver functions as well as that on theoretical seismograms. Linear transformation of fast and slow components of the split *Ps* phase yields the radial and transverse receiver functions of the *Ps* phase, $r_r(t)$ and $r_t(t)$,

$$r_r(t) = V_2(t) \cos 2\phi + V_1(t) \cos \phi + V_0(t),$$
$$r_t(t) = W_2(t) \sin 2\phi + W_1(t) \sin \phi,$$
(9)

where ϕ denotes the back azimuth measured from the horizontal-symmetry axis or horizontal projection of inclined symmetry axis, and $V_0(t)$, $V_1(t)$, $V_2(t)$, $W_1(t)$, and $W_2(t)$ are dependent on the velocity profile, anisotropy parameters, and ray geometry. In the case of the horizontal-symmetry axis, equation (9) is written as
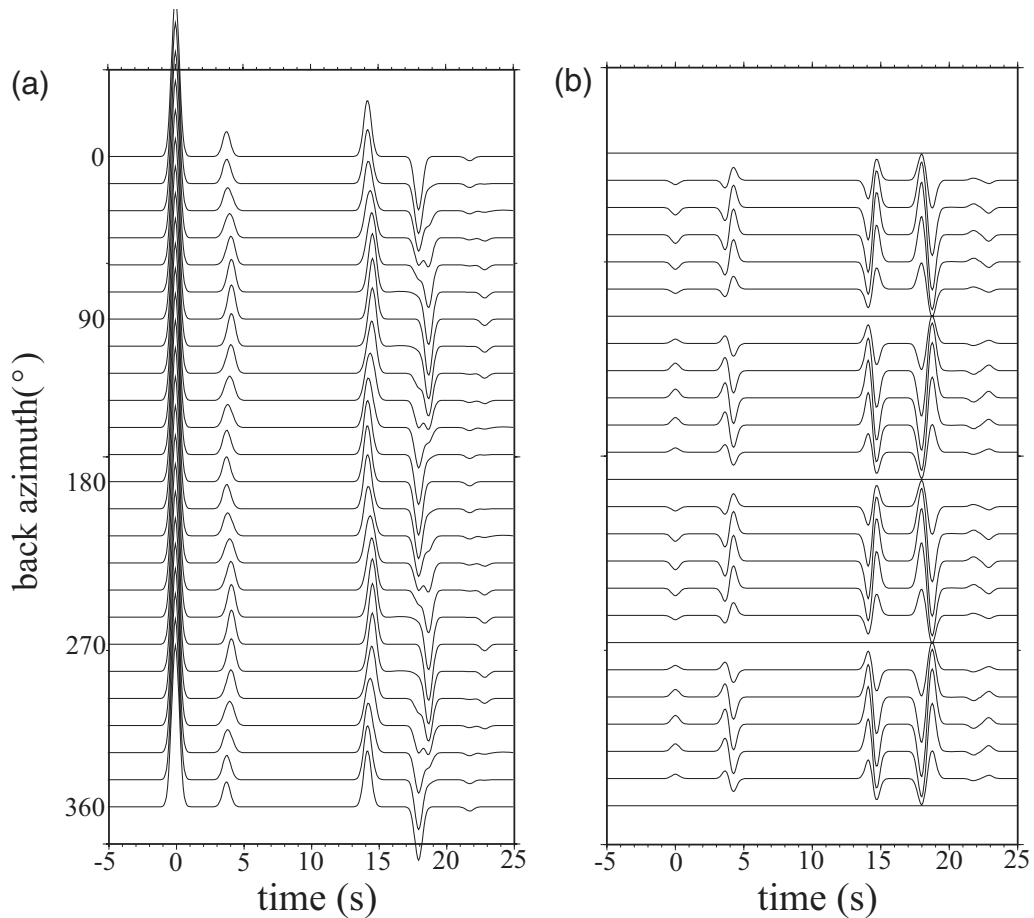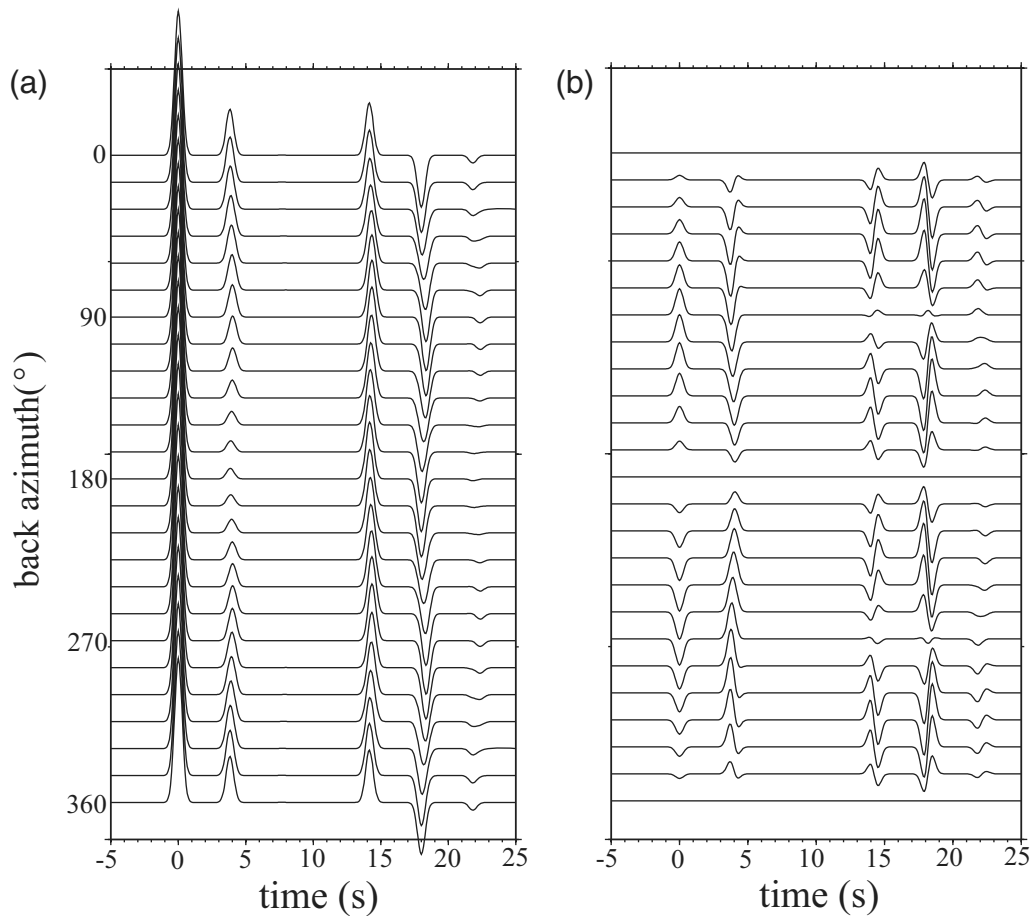
Figure 2. Receiver functions for Model 1a lined up in order of increasing ray back azimuth: (a) radial component and (b) transverse component. Transverse component amplitude is scaled up with factor of 2.

$$r_r(t) = a(t + \delta t/2)(\cos \phi)^2 + a(t - \delta t/2)(\sin \phi)^2,$$
$$r_t(t) = -\{a(t + \delta t/2) - a(t - \delta t/2)\} \sin \phi \cos \phi, \tag{10}$$

where $a(t + \delta t/2)$ and $a(t - \delta t/2)$ denote the receiver function waveforms of fast and slow components of the split Ps phase, respectively, and δt is the time lag between their arrivals. The transverse receiver functions in Figure 2 show that the initial motions of direct P wave and Ps-converted wave have the same polarity and that their amplitude variations versus ϕ exhibit a four-lobed pattern ($\sin 2\phi$), which can be easily understood by using equation (10). Thus, the direct P wave and Ps phase disappear when the incident direction is parallel or normal to the hexagonal-symmetry axis in the north. The four-lobed pattern of amplitude variation is also seen in the reverberated later phases. On the other hand, the Ps phase on the radial receiver function shows the azimuthal amplitude variation that would be expressed by $a(t) - \delta a(t) \cos 2\phi$, which is an approximate expression of equation (10). In addition, peak arrival time of the Ps phase versus ϕ exhibits four-lobed modulation that would be written as $t_0 - \delta t \cos 2\phi$, where t_0 denotes the reference arrival time. The arrival-time modulation can be understood when

the amplitude variation of $a(t) - \delta a(t) \cos 2\phi$ is taken into account. But the arrival-time modulation is not seen in the Ps phase on the transverse component because the transverse Ps waveform in equation (10) is approximately expressed by $\delta a(t) \sin 2\phi$.

Figure 3 shows radial and transverse receiver functions for Model 1b, in which the hexagonal-symmetry axis is inclined toward the north (see Table 1). On the transverse receiver functions, the amplitude variations of direct P wave and Ps phase show a two-lobed pattern depending on $\sin \phi$, where ϕ is measured from the horizontal projection of the inclined symmetry axis. In particular, the Ps-phase amplitude becomes maximum when the ray is normal to the symmetry axis direction and disappears when it is parallel to the symmetry axis. The four-lobed pattern is also observed in the amplitude variation of the reverberated later phases, and this amplitude variation is always seen for the later phases irrespective of inclination of the hexagonal-symmetry axis in the surface layer. The Ps-phase amplitude on the radial receiver function is maximum at $\phi = 0$ and minimum at $\phi = 180°$. These variations of Ps-phase amplitude versus ϕ are easily understood by taking into account that the $\sin 2\phi$ and $\cos 2\phi$ terms in equation (9) are much smaller than $\sin \phi$, $\cos \phi$, and
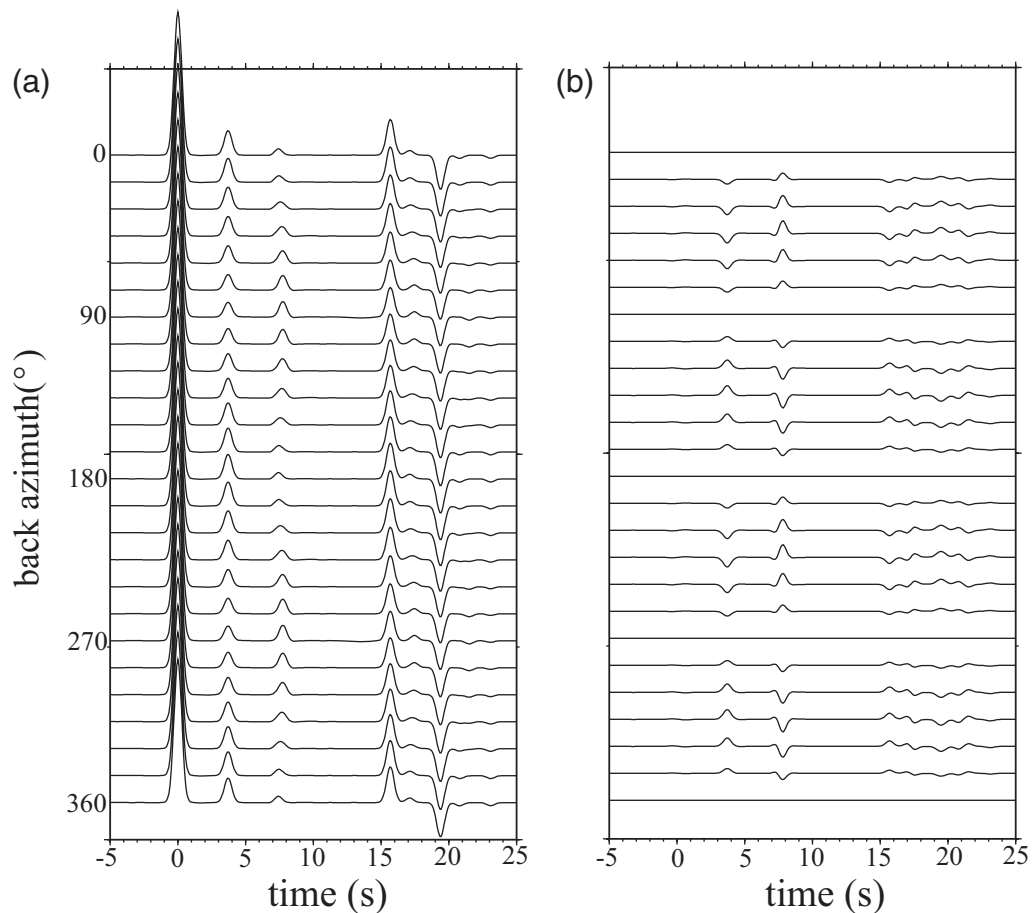
Figure 3. Receiver functions for Model 1b lined up in order of increasing ray back azimuth: (a) radial component and (b) transverse component. Transverse component amplitude is scaled up with factor of 2.

constant terms. The characteristics of *Ps*-phase amplitude variations are basically consistent with results shown by Savage (1998). We think that the systematic amplitude change of *Ps* phase is available for determining the orientation of the hexagonal-symmetry axis in the anisotropic layer.

Figure 4 depicts radial and transverse receiver functions for the three-layered anisotropic structure (Model 2a), which consists of an isotropic surface layer, an anisotropic middle layer, and an isotropic bottom layer (see Table 2). On the radial receiver functions, the first arrival phase is a direct *P* wave and the second and third phases are *Ps*-converted waves at the top and bottom interfaces of the middle layer, respectively. The direct *P* wave disappears on the transverse receiver function, but the two *Ps* phases converted at the middle layer are clearly identified on the transverse and radial receiver functions. Particle motion on the horizontal plane is linear for the first *Ps* phase and nonlinear for the second *Ps* phase. Thus, the first *Ps* phase does not exhibit the characteristic of shear-wave splitting, whereas the second *Ps* phase takes on the shear-wave polarization anisotropy during propagation into the anisotropic middle layer. The reason why the shear-wave splitting does not happen to the first *Ps* phase is because the *Ps* phase only travels into

the isotropic surface layer. On the transverse receiver function, amplitude variations of the first *Ps* and second *Ps* phases exhibit a four-lobed pattern ($\sin 2\phi$), and their waveforms and polarities are quite similar to those of the direct *P* wave and *Ps* phase in the case of Model 1a. On the radial component, the arrival time of the peak amplitude of the first *Ps* phase is constant at all ray back azimuths because the surface layer is isotropic, but that of the second *Ps* phase varies with a change in ray back azimuth because of the seismic anisotropy in the middle layer. The arrival-time modulation of the second *Ps* phase is similar to that of the *Ps* phase of the radial receiver functions in the case of Model 1a. These results imply that the splitting of the *Ps* phase is controlled by seismic anisotropy in the layers above the velocity discontinuity, which causes the *Ps* conversion.

Receiver functions for Model 2b are shown in Figure 5. Note that the symmetry axis is inclined in the middle layer (Table 2). The azimuthal variation of the transverse receiver function is similar to that in the case of Model 1b, but there is a distinct difference between the radial receiver functions calculated for Models 1b and 2b. The radial receiver function shows that the polarity of the second *Ps* phase is reversed within a range of ray back azimuth. In the case of the layered

Figure 4. Receiver functions for Model 2a lined up in order of increasing ray back azimuth: (a) radial component and (b) transverse component. Transverse component amplitude is scaled up with factor of 2.

isotropic structure, the *Ps*-converted phase on the radial receiver function usually has positive polarity when the *P* wave is traveling across a velocity discontinuity from the high-velocity side to the low-velocity side; it exhibits negative polarity in the reverse case where the *P* wave is propagating from the low-velocity side to the high-velocity side. This feature was utilized to discover a low-velocity layer just above the oceanic plate from the polarity of the *Ps*-converted wave (Sacks and Snoke, 1977; Nakanishi, 1980; Oda and Douzen, 2001). However, when seismic anisotropy resides in layers above a velocity discontinuity, the *Ps*-phase polarity is reversed within a range of back azimuth (Fig. 5). Thus, one should take into account the seismic anisotropy when finding a low-velocity zone from polarity of the converted waves on radial receiver function.

Receiver functions for the three-layer model (Model 3) are illustrated in Figure 6. In the upper two layers of the model, the hexagonal-symmetry axes are oriented in arbitrary directions (Table 3). Reversal of *Ps*-phase polarity is observed on the radial receiver functions in a range of back azimuth. The *Ps*-phase amplitude variations versus ray back azimuth, in comparison with those shown Figures 4 and 5, are complicated by the arbitrary orientation of the symmetry

axis in the layers above and below the velocity discontinuities. In this case, it is not easy to estimate the anisotropic structure from the variation pattern of the *Ps*-receiver function waveforms versus ray back azimuth.

Shear-Wave Splitting Analysis of the *P*-Wave Receiver Function

The *P*-wave receiver functions of layered anisotropic structure indicated that *Ps*-converted phases and other later phases exhibit characteristics of shear-wave splitting in a similar way to polarization anisotropy of direct *S* waves from earthquake sources (e.g., Fig. 2). The splitting is seen in a particle motion diagram on the horizontal plane as a deviation from a linear particle motion predicted by isotropic theory. The shear-wave splitting is described by two parameters: the time lag δt between two arrivals of split shear wave and the polarization direction ϕ_s of the fast arrival component (e.g., Ando *et al.*, 1980). The fast polarization direction ϕ_s is related to the orientation of the hexagonal-symmetry axis; the time lag δt represents anisotropy intensity. In the case of the horizontal-symmetry axis, ϕ_s is equal to azimuth λ of the symmetry axis if *E* in equation (1) is positive, and ϕ_s
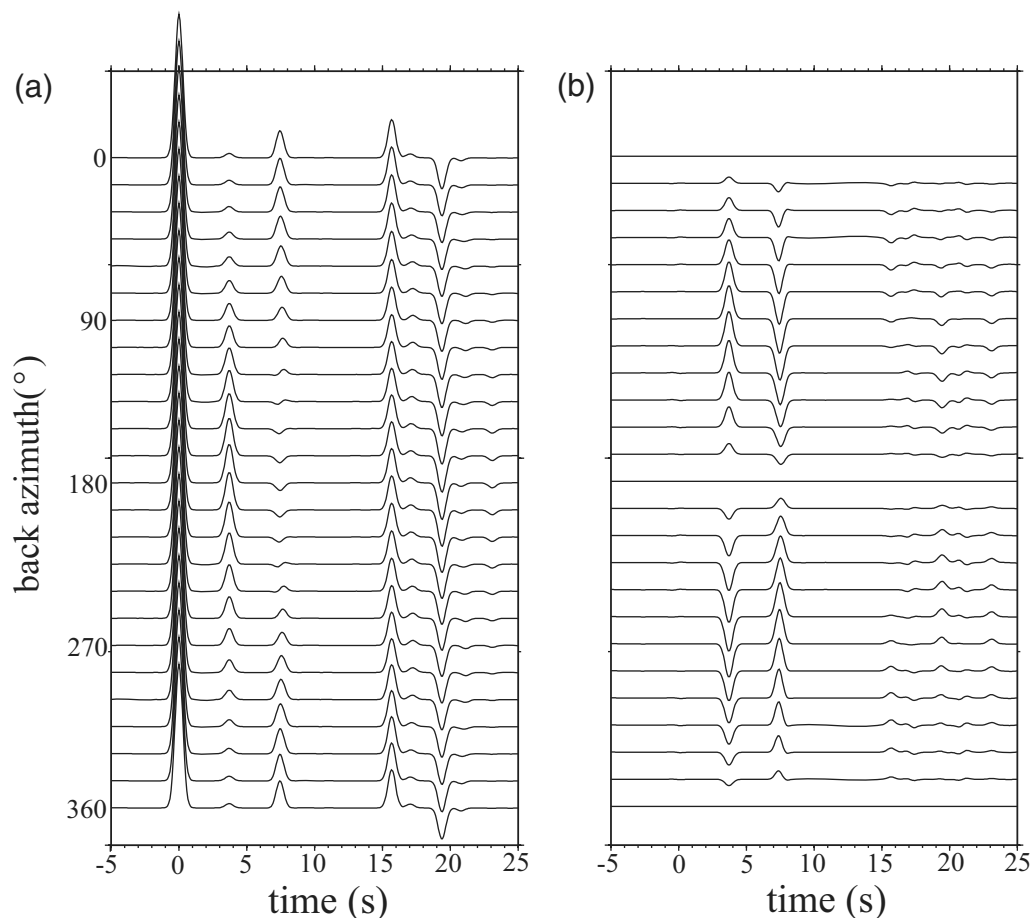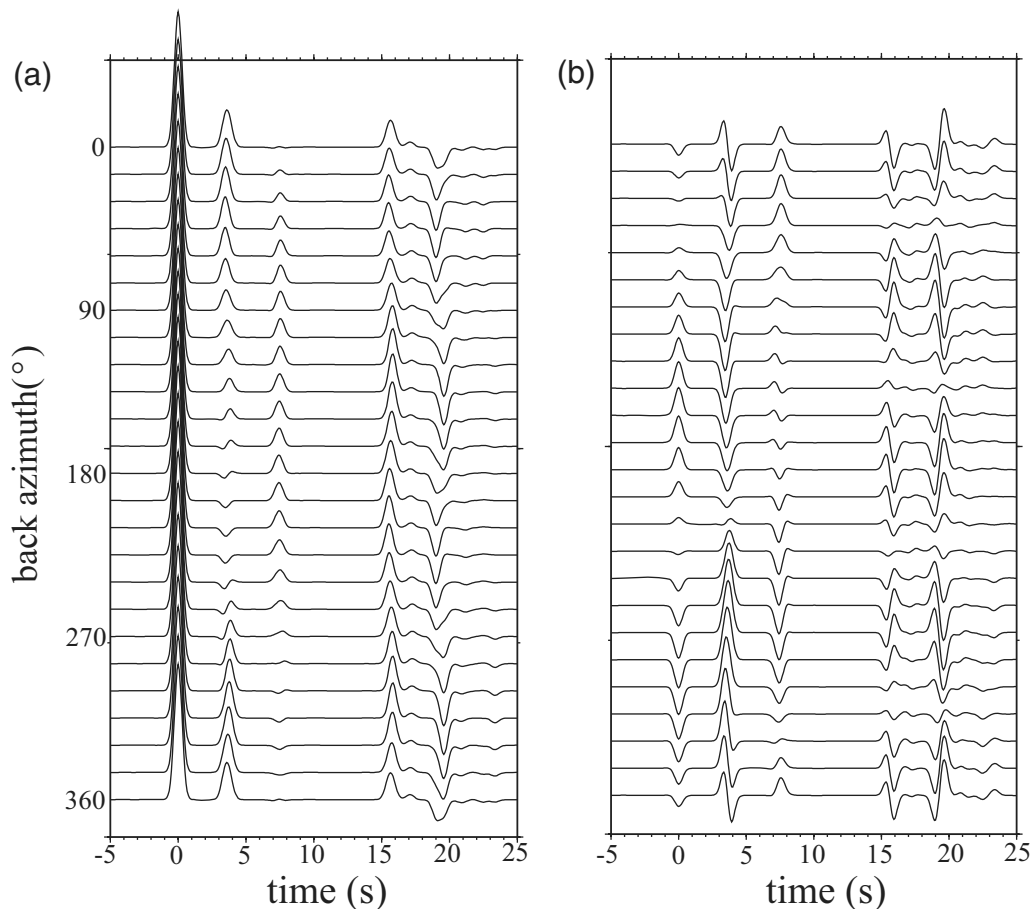
Figure 5. Receiver functions for Model 2b lined up in order of increasing ray back azimuth: (a) radial component and (b) transverse component. Transverse component amplitude is scaled up with factor of 2.

agrees with $\lambda + 90°$ if E is negative. The hexagonal symmetry caused by stress-induced cracks corresponds to the latter case, where the hexagonal-symmetry axis is normal to the crack plane (Anderson, 1989). When the shear wave splits due to aligned vertical cracks in the crust, the fast polarization direction agrees with the direction of the crack alignment or tectonic stress that leads to it, and the time lag is in proportion to the crack density. Thus, estimating the splitting parameters is important when studying the tectonic stress field in the crust and the mantle dynamics, which are inferred from orientation of the symmetry axes. Hence we try to estimate the splitting parameters by shear-wave splitting analysis of Ps phases on radial and transverse receiver functions. There are basically two methods to estimate ϕ_s and δt from receiver functions: one is the waveform cross-correlation method (Ando *et al.*, 1980) and the other is the splitting operator method (Silver and Chang, 1991). In this study, we employ the former method and use the latter method to examine the reliability of the estimated splitting parameters.

In order to verify that ϕ_s and δt can be estimated by the waveform cross correlation of Ps-receiver functions, we perform numerical experiments using synthetic receiver functions calculated for the three-layered anisotropic structure

(Model 3). The synthetic receiver functions for the P wave incoming from the north are shown in Figure 7, where the first Ps phase converted at the shallow velocity discontinuity appears around 4 sec after the first P arrival time. The Ps-phase waveforms are taken out from the radial and transverse receiver functions by a boxcar time window of 4 sec. The contour plot of the cross-correlation coefficient between the windowed Ps waveforms is shown as a function of ϕ_s and δt (Fig. 8). The ϕ_s and δt at which the coefficient becomes maximum are best estimates of the fast polarization direction and the time lag of the splitting Ps phase. We obtain $\phi_s = 38°$ and $\delta t = 0.30$ sec from the contour plot in Figure 8. They are nearly equal to the values of splitting parameter predicted from the anisotropic velocity parameters of the surface layer of Model 3. It is interesting that the value of ϕ_s close to the given azimuth $\lambda = 40°$ is obtained though the hexagonal-symmetry axis that is inclined in the surface layer (see Table 3). Fast (ϕ_s direction) and slow ($\phi_s + 90°$ direction) components of the receiver functions are shown in Figure 7. The waveforms of the first Ps phases on both components have similar shape, indicating that the particle motion is linear on the horizontal plane. Further, we correct the receiver functions for the splitting operator that is calcu-
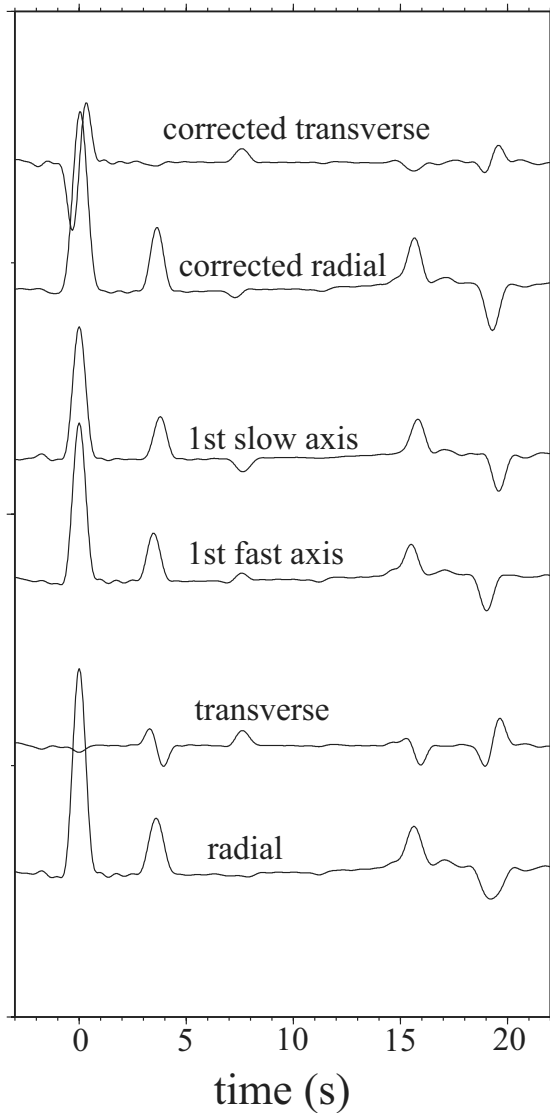
Figure 6.   Receiver functions for Model 3 lined up in order of increasing ray back azimuth: (a) radial component and (b) transverse component. Transverse component amplitude is scaled up with factor of 2.

lated using the estimated ϕ_s and δt (Silver and Chang, 1991). The first Ps phase disappears from the corrected transverse component of the receiver function (see Fig. 7). This means that the anisotropy effect of the surface layer is removed from the radial and transverse receiver functions. On the corrected receiver functions, another seismic phase is identified around 8 sec after the first P arrival time. This phase is identified as the second Ps phase converted at the velocity discontinuity between the middle and bottom layers (see Table 3), and it informs us about the seismic anisotropy of the middle layer because the anisotropy of the surface layer was corrected for the second Ps phase. The splitting parameters of the second Ps phase are estimated by the same splitting analysis as the first Ps phase, and we obtain $\phi_s = 158°$ and $\delta t = 0.28$ sec from the waveform cross-correlation diagram. The estimated values of the splitting parameters are basically close to those predicted from the anisotropic velocity parameters of the middle layer of Model 3. The small difference between the values of ϕ_s and λ may result from the inclination of the symmetry axis. When the symmetry axis is horizontal, the estimated ϕ_s is confirmed to agree with the given azimuth $\lambda = 150°$. Therefore, the splitting analysis of Ps phases on

receiver functions is available for an estimate of the depth variation of seismic anisotropy.

We consider a limit of application of the splitting analysis to Ps-converted phases. Figure 9 shows receiver functions calculated for the three-layered structure, where a very thin anisotropic layer is sandwiched by two isotropic layers. Thickness of the middle layer is 3 km, and the other model parameters are the same as those of Model 2a. In comparison with the receiver functions for Model 2a (Fig. 4), the waveform variation of the radial component versus the back azimuth is not clear, and the Ps-phase amplitude of the transverse component is very small. In addition, the first and second Ps phases that are generated at the top and bottom interfaces of the thin middle layer are overlapping, and they look like a single Ps phase converted at a velocity discontinuity. These characteristics of receiver functions are very similar to those for the two-layered isotropic structure. In this case, it would be difficult to recognize from the receiver functions that there is a thin anisotropic layer in the structure. Levin and Park (1998) and Savage (1998) pointed out that a thin layer P-to-S conversion might be an impediment to correctly measuring the shear-wave polarization anisotropy by the shear-wave splitting method. Nevertheless, we tried to

Figure 7. Synthetic receiver functions calculated for Model 3: transverse and radial component for *P*-wave incidence (bottom two traces), fast (ϕ_s direction) and slow ($\phi_s + 90°$ direction) components of *Ps*-receiver functions (middle two traces), and transverse and radial receiver functions corrected for the splitting factor in the surface layer (top two traces).

estimate the splitting parameters from the cross-correlation diagram of the overlapped *Ps* phases on the receiver functions, and we obtained $\phi_s = 24°$ and $\delta t = 0.16$ sec. As we have thought, they are not in agreement with $\lambda = 40°$ and $\delta t = 0.04$ sec that were predicted from the anisotropic parameters of the thin layer. Thus, one should take into account that the splitting analysis is not applicable to the *Ps* phases converted by a very thin anisotropic layer.

Next, we examine how inclination of the hexagonal-symmetry axis has influence on the estimate of splitting parameters. For this purpose, we produce artificial receiver functions of two-layer structures consisting of an isotropic bottom layer and an anisotropic surface layer with an in-

clined symmetry axis. In the two-layered structure, we set $\lambda = 40°$ and assign different values to the axis tile angle ξ. We determine ϕ_s and δt by the splitting analysis of *Ps* phases on the produced receiver functions. The estimated splitting parameters are plotted versus the axis tilt angle ξ (Fig. 10). The azimuth ϕ_s varies with increasing tilt angle, but it is close to $\lambda = 40°$ at larger tilt angles. This change of the estimated ϕ_s versus ξ may arise because the split components of the *Ps*-converted wave cannot be completely separated by rotation of the radial and transverse receiver functions on the horizontal plane. As an observation error of ϕ_s estimated by the waveform cross-correlation method was around $\pm 10°$ (e.g., Bowman and Ando, 1987), the splitting analysis may be available for the axis tilt angle larger than 30°. On the other hand, the time lag δt decreases with decreasing the axis tilt angle and vanishes in the case of vertical symmetry axis, that is, the transversely isotropic case (Fig. 10). A simple calculation using equation (1) under the assumption of $C = 0$ yields an approximate expression of the time lag

$$\delta t = LE(1 - \cos 2\eta)/2\beta_0, \tag{11}$$

where L is the traveling distance of the *Ps* phase in the surface layer. Since the ray path of the *Ps* phase is nearly vertical in the surface layer, the angle η is approximately equal to the axis tilt angle ξ. The theoretical curve of the time lag calculated using equation (11) is shown as a function of ξ in Figure 10. The theoretical curve is close to the time lags estimated by the splitting analysis, indicating that δt is reliably estimated even if the symmetry axis is inclined. When the symmetry axis is approximately vertical, the elastic behavior of the surface layer is transversely isotropic. In this case, the shear-wave splitting of the *Ps* phase becomes unclear because the excitation of the transverse component by the *P-SH* conversion is weak; consequently, it is difficult to precisely determine the splitting parameters.

Real Splitting Analysis of *Ps* Phases on the Receiver Functions

We execute real analysis of receiver functions using teleseismic waveform data recorded at four *F*-net and two temporal stations in the Chugoku district, southwest Japan (see Fig. 11). At the two temporal stations, a velocity-type seismometer with 1 or 5 sec in natural period is installed. The waveform data are digitized at sampling rate of 20 or 50 Hz with a 12-bit resolution. On the other hand, the seismic stations of *F*-net, which is a broadband seismic network deployed over Japan, are equipped with STS-1 or STS-2-type broadband velocity seismometers. The waveform data are digitized at a 20 Hz sampling rate with a 24-bit resolution. We calculate the radial and transverse receiver functions, using the waveform data from 100 teleseismic earthquakes whose epicenters are plotted in Figure 12. Random noise is removed from the receiver functions by a singular value decomposi-
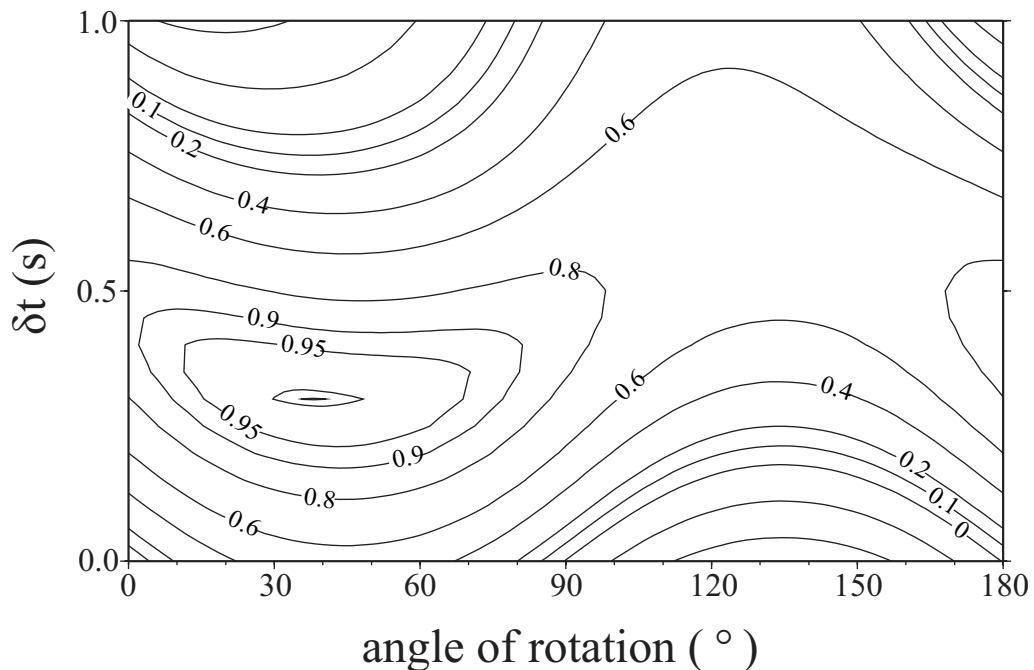
Figure 8. Contour plot of the cross-correlation coefficient between the radial and transverse receiver functions of the split *Ps* phase as a function of ϕ_s and δt. Numbers tagged to contours indicate values of the cross-correlation coefficients.

tion filter (Chevrot and Girardin, 2000) for which the largest five eigenvalues are adopted. As an example, the filtered receiver functions at YZK (see Fig. 11) are shown for the selected earthquakes in order of increasing ray back azimuth (Fig. 13). The *Ps*-converted phase clearly appears at about 5 sec after the first *P* arrival time on all receiver functions, so it is considered to be generated at the Moho discontinuity.

We take out the *Ps*-phase waveforms from the radial and transverse receiver functions by a boxcar time window of 3 to 5 sec and estimate the splitting parameters, ϕ_s and δt, by the waveform cross-correlation analysis of the windowed *Ps* phases. The observed receiver functions are corrected for the splitting factor that is obtained using the estimated ϕ_s and δt, in a similar way to Silver and Chang (1991). When the *Ps* phase does not disappear on the corrected transverse receiver function, the estimated splitting parameters are discarded. The frequency of ϕ_s is plotted versus azimuth on the Rose diagram (Fig. 14). We define the fast polarization direction by the azimuth at which a frequency of ϕ_s is maximum. Figure 11 shows the fast polarization directions obtained at six stations in the Chugoku district. Because the *Ps* phase analyzed is thought to stem from the *Ps* conversion at the Moho discontinuity, the estimated splitting parameters reflect the anisotropy inside the crust. The average of the time lags and the fast polarization direction at each station are listed in Table 4. The averaged δt is from 0.2 to 0.7 sec and seems to be somewhat larger than the representative values of the time lag in the crust of Japan Islands (see Kaneshima, 1991). The representative values basically reflect the intensity of seismic anisotropy in the upper crust because they were estimated using the direct *S* wave from

local earthquakes that occurred in the upper crust, whereas the splitting parameters of the *Ps* phases generated at the Moho represent anisotropic properties of the entire crust. This difference may give rise to the disagreement between the time lags estimated from the direct *S* wave and the *Ps* phase. Figure 11 shows that the fast polarization directions in the crust are in the trend of north–south to northeast–southwest. Iidaka (2003) determined the fast polarization directions by a splitting analysis of multiple-reflected shear waves within the crust and emphasized that the fast polarization directions of the crust were from north–south to northeast–southwest (see Fig. 11). Our estimate of ϕ_s is consistent with that in Iidaka's study. Further, a recent study reported that *P* waves in the crust of the Chugoku district have an azimuthal anisotropy of the fast propagation direction in north–south to northeast–southwest (Ishise and Oda, 2008). These results demonstrate validity of the estimate of the splitting parameters by means of the splitting analysis of *Ps*-phase waveforms on the receiver functions.

Several causes are considered for seismic anisotropy; (1) lattice preferred orientation of anisotropic crystals, (2) alignment of melt-filled cracks, (3) alignment of cracks induced by regional tectonic stress, and (4) internal deformation by a past tectonic process. The first two are available to explain the upper mantle anisotropy and the mantle wedge anisotropy within the subduction zone (e.g., Crampin, 1981; Iidaka and Obara, 1995; Oda and Shimizu, 1997; Hiramatsu *et al.*, 1998) and they are thought to give rise to a fairly large anisotropy. Thus, the crystal-preferred orientation and the melt-filled cracks may not be appropriate for a primary cause of the crustal anisotropy. If alignment of stress-induced
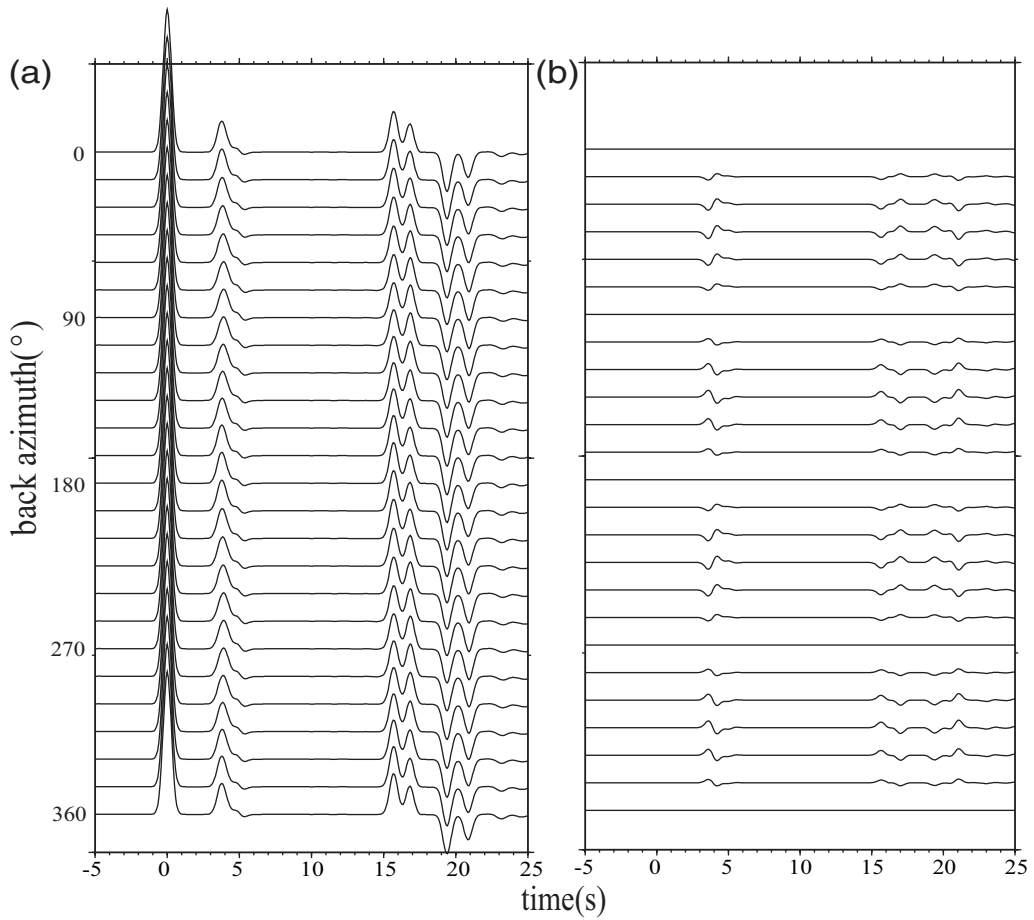
Figure 9. Receiver functions in order of increasing ray back azimuth: (a) radial component and (b) transverse component. They are calculated for a three-layered anisotropic structure similar to Model 2a, where a very thin anisotropic layer is sandwiched by two isotropic layers. Transverse component amplitude is scaled up with factor of 2.
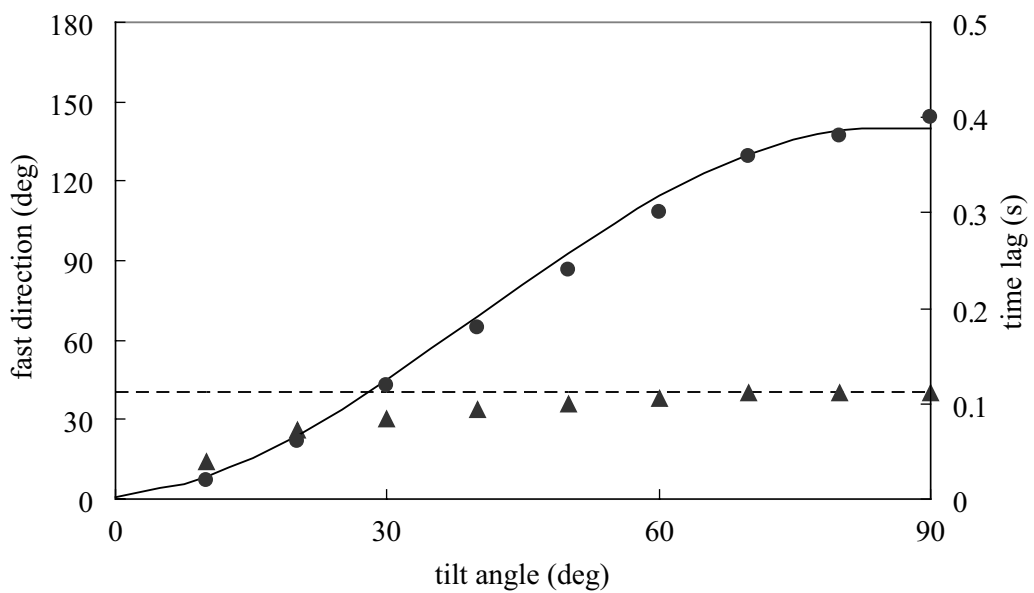

Figure 10. Changes of fast polarization direction ϕ_s (triangle) and time lag δt (circle) versus tilt angle ξ of a hexagonal-symmetry axis. Right and left ends correspond to horizontal and vertical symmetry axes, respectively. Theoretical δt calculated by equation (9) are shown by curve. The dashed line indicates $\lambda = 40°$.
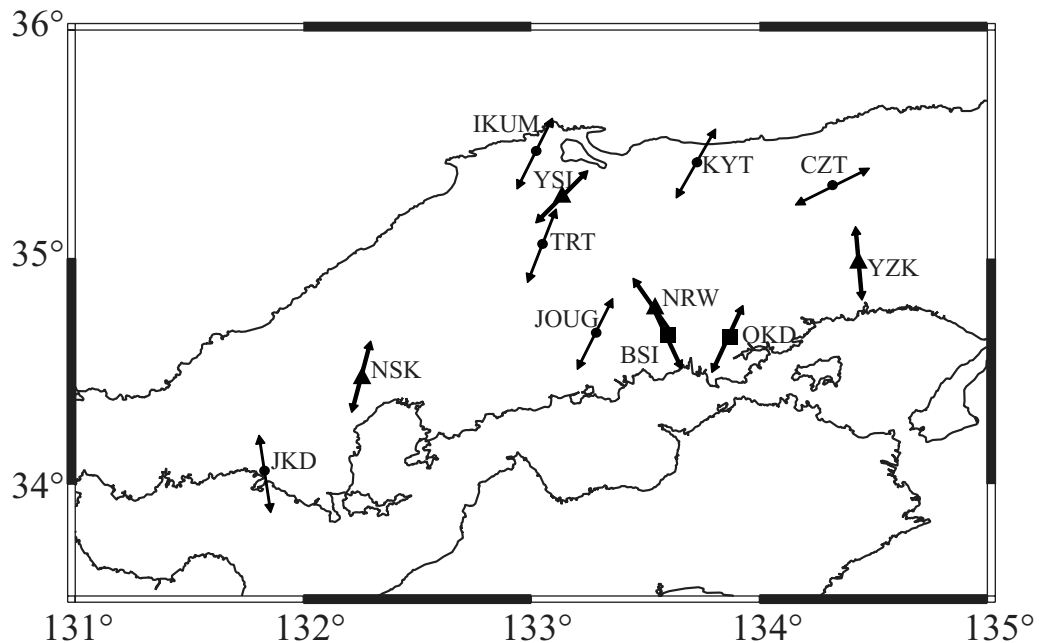
Figure 11. Locations of seismic stations and the fast polarization directions (thick arrows) obtained from receiver functions of the Moho-generated *Ps* phase. The fast polarization directions that Iidaka (2003) determined from the splitting of the shear waves reverberated in the crust are shown by thin arrows. Triangles and squares indicate locations of *F*-net and temporal stations used in this study, respectively. Circles represent locations of seismic stations used in the Iidaka study.

cracks is a preferable cause for the seismic anisotropy in the crust, then the fast polarization direction is expected to be a northwest–southeast trend that is the direction of maximum principal stress in southwest Japan (e.g., Tukahara and Kobayashi, 1991). However, our estimate shows the fast
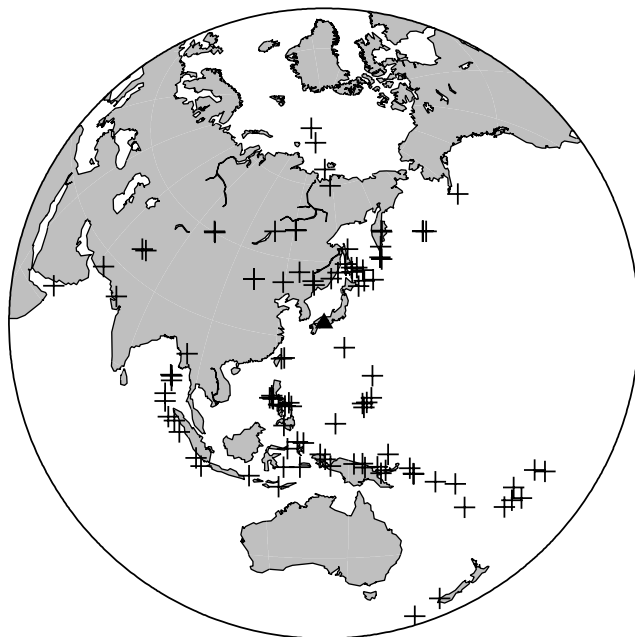
Figure 12. Distributions of earthquake epicenters (cross) used for real receiver function analysis. The triangle shows the representative location of seismic stations. Hypocenter data of earthquakes were collected from the Global CMT Catalog (see Data and Resources section).

polarization direction to be from north–south to northeast–southwest. Thus, the cracks induced by regional tectonic stress are not appropriate for the cause that leads to the crustal anisotropy estimated in this study. Silver and Chang (1991) measured the seismic anisotropy beneath the continents by a shear-wave splitting method and attributed it to internal deformation of the mantle or continental plate by a past tectonic process such as orogeny. Such a deformation process might produce a geological lineament structure inside of the crust. In southwest Japan, there is some geological evidence to support the lineament structure in the direction of the northeast–southwest trend (Iidaka, 2003). For example, the epicenter distributions of crustal earthquakes in west Japan delineate clear line segments in the northeast–southwest direction trend (Nakamura *et al.*, 1997), and most of the active faults are observed elongating in the northeast–southwest trend (e.g., The Research Group for Active Faults of Japan, 1991). Because the trend of the linear epicenter distributions and the active fault strikes are basically in agreement with the fast polarization directions of the *Ps* phases, the measured polarization anisotropy might be caused by the lineament structure inside of the crust.

Finally, we examine a possibility that the dipping boundary of isotropic layers excites *Ps*-converted phases on transverse and radial component receiver functions. The receiver function from the dipping boundary shows two important characteristics: a systematic variation of *Ps*-phase waveforms versus ray back azimuth and the appearance of seismic energy on both the radial and transverse components (e.g., Girardin and Farra, 1998; Savage, 1998). These char-
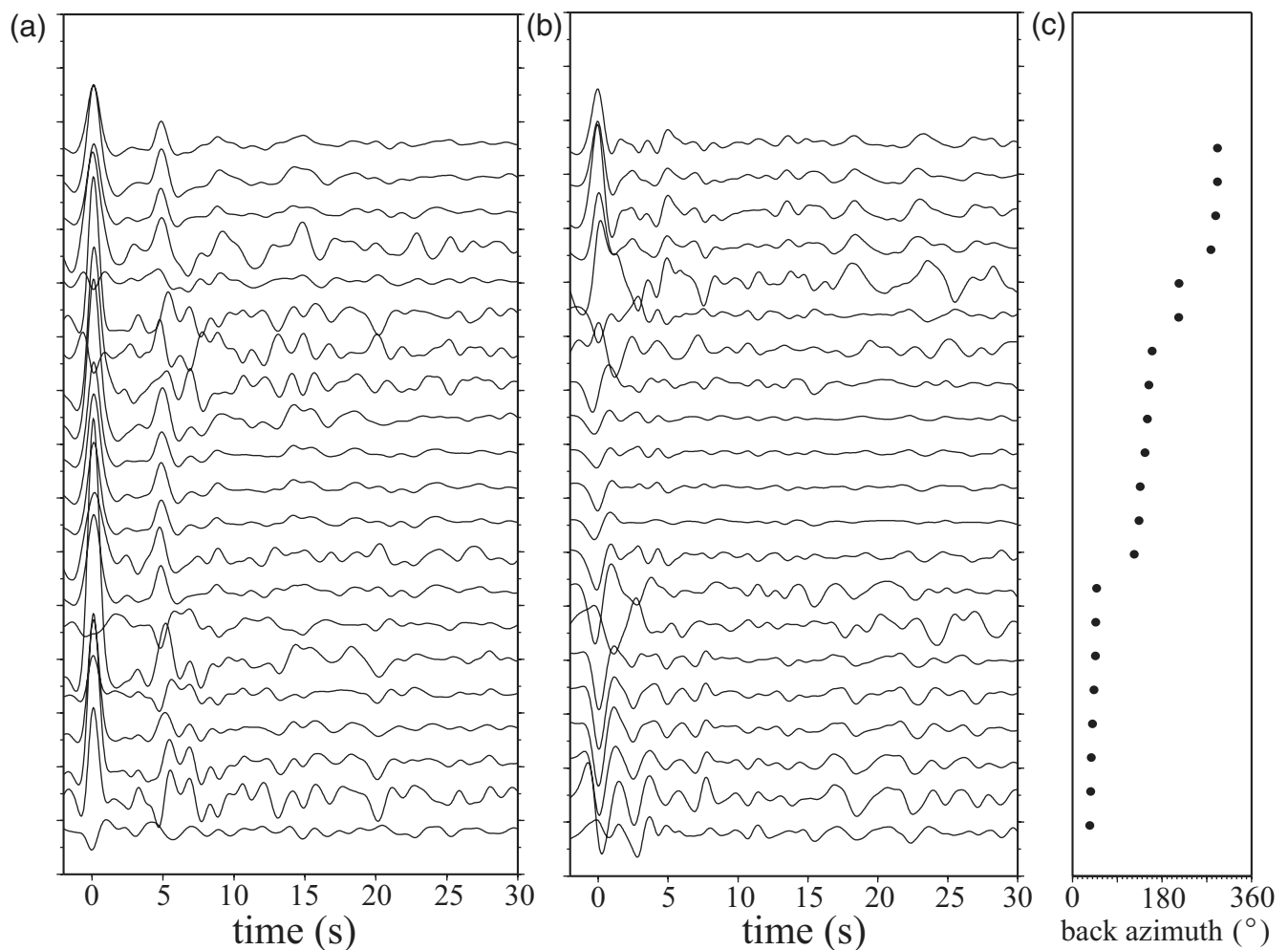
Figure 13. Receiver functions obtained from selected seismograms at YZK: (a) radial component, (b) transverse component, and (c) ray back azimuths to earthquake epicenters.

acteristics are very similar to those seen on receiver functions of stratified anisotropic structure. An approach to distinguish between the effects of dipping boundary and seismic anisotropy on the receiver function is the phase delay between the *Ps* phases on radial and transverse components. The particle motion diagram of the *Ps* phases is nonlinear due to the phase delay when shear-wave splitting happens to the *Ps* phases, whereas it shows a linear motion in the case of the dipping boundary (Kamimoto, 2007). This result means that no delay time δt may be measured in the case of the dipping boundary of an isotropic layer. Because we measured the delay times at six stations, the appearance of the *Ps* phases on the transverse component would not be attributable to the dipping isotropic layers.

Conclusions

We investigated the effect of seismic anisotropy on *P*-wave receiver functions, calculating synthetic seismograms for *P*-wave incidence on a multilayered anisotropic structure with hexagonal symmetry. We verified on the receiver functions that the waveforms of *Ps*-converted phases propagating the anisotropic layers have the characteristic of shear-wave splitting. The shear-wave splitting was also observed in later phases reverberated as shear wave in the anisotropic layers. On the radial receiver function of the two-layered structure that consists of an isotropic bottom layer and an anisotropic surface layer with a horizontal-symmetry axis, the arrival time of the *Ps*-phase peak amplitude showed the variation of a four-lobed pattern versus ray back azimuth ϕ of incident *P* wave, while on the transverse receiver function, the *Ps*-phase arrival time was independent of ϕ. On the other hand, the amplitudes of *Ps* phases and other later phases varied with a change in ϕ because of the shear-wave splitting, depending on the anisotropic properties specified by orientation of the hexagonal-symmetry axis and anisotropy intensity. The radial receiver functions revealed that the *Ps*-phase polarity is reversed in a range of ϕ and the variation pattern of *Ps*-phase amplitude versus ϕ is dependent on the inclination of the symmetry axis. On the transverse receiver function, the *Ps*-phase amplitude varied versus ϕ with a four-lobed pattern for a horizontal-symmetry axis
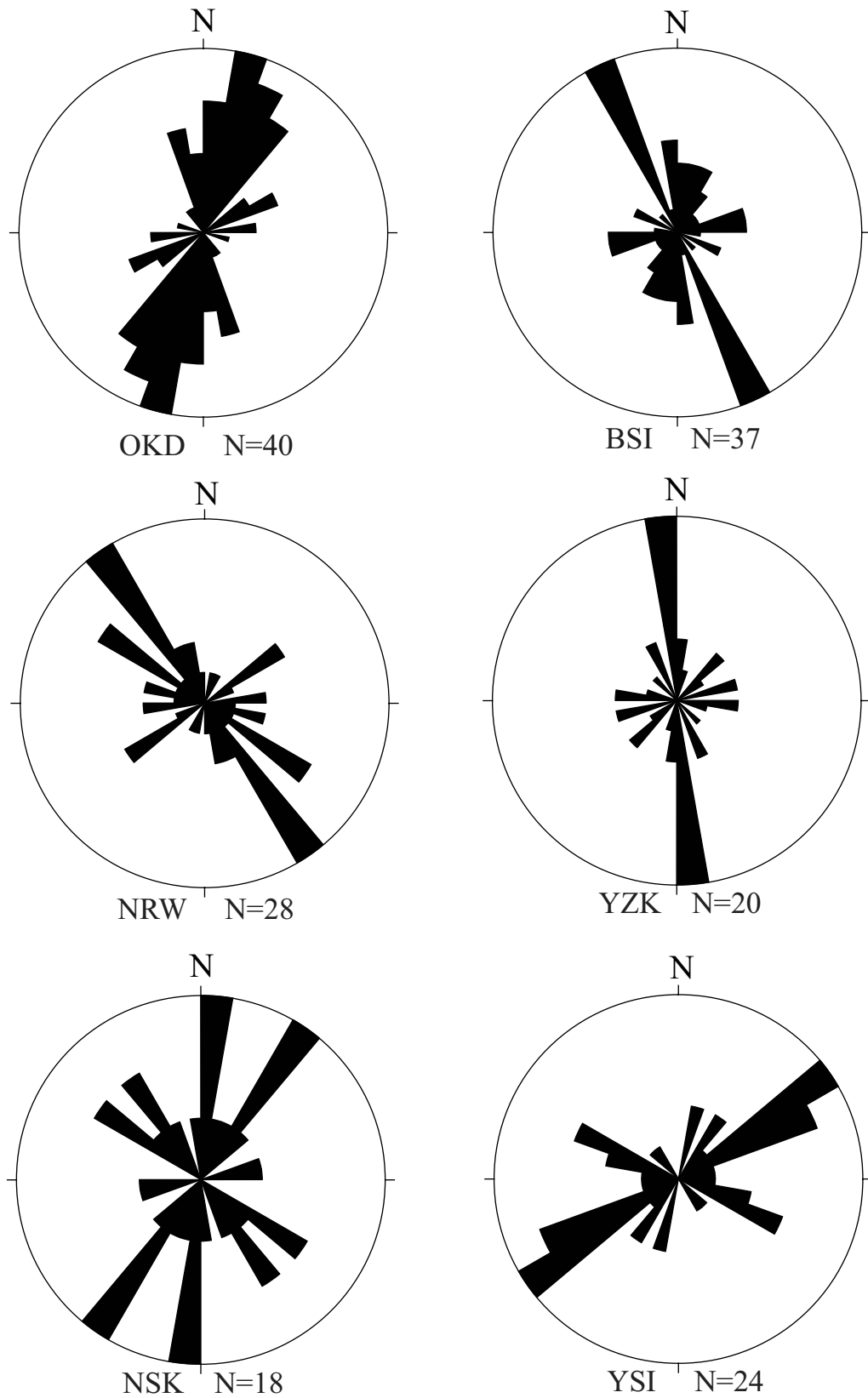
Figure 14. Rose diagrams of fast polarization directions estimated at six seismic stations. *N* denotes the number of plotted data.

Table 4
Averaged Values of ϕ_s and δt_s

	OKD	BSI	NRW	YZK	YSI	NSK
ϕ_s (°)	24.5 ± 3.1	-24.0 ± 2.3	-35.8 ± 2.8	-4.4 ± 3.2	54.7 ± 2.9	19.6 ± 15.4
δt (sec)	0.75 ± 0.18	0.16 ± 0.09	0.53 ± 0.32	0.23 ± 0.20	0.21 ± 0.22	0.74 ± 0.18

and with a two-lobed pattern for an inclined symmetry axis, but the amplitude variation of the reverberated later phases always showed a four-lobed pattern, irrespective of the axis inclination. These amplitude variations of the *Ps* phase were complicated by arbitrary orientation of hexagonal-symmetry axes in the three- or more-layered anisotropic structure.

We demonstrated that the fast polarization direction ϕ_s and the time lag δt can be estimated by the waveform cross-correlation analysis of *Ps* phases on radial and transverse receiver functions when hexagonal-symmetry axes are not largely inclined from the horizontal plane. In addition, the splitting analysis was shown not to be applicable to the *Ps* phase generated by a very thin anisotropic layer. Real splitting analyses were performed on the radial and transverse receiver functions that were obtained from teleseismic waveforms at six stations in the Chugoku district, southwest Japan. Clear *Ps* phases, which were considered to be converted at the Moho discontinuity, were identified around 5 sec after the first *P* arrival time on the receiver functions. The splitting analysis of the *Ps*-phase waveforms showed the fast polarization directions to be approximately in the north–south to northeast–southwest direction inside of the crust. This result was consistent with recent results of shear-wave splitting measurements and the trend of linear epicenter distributions of crustal earthquakes and the active fault strikes in the Chugoku district, but it was inconsistent with trajectories of maximum principal stress acting on southwest Japan. The crustal anisotropy was interpreted as being attributable to the geological lineament structure, which is an internal deformation in the crust by past tectonic process.

Data and Resources

Seismograms used in this study were collected from *F*-net operated by the National Research Institute for Earth Science and Disaster Prevention and are released to the public. Most of plots were made using the Generic Mapping Tools (GMT) version 3.3.6 (Wessel and Smith, 1991). Hypocenter data of earthquakes were collected from the Global Centroid Moment Tensor (CMT) Catalog (www.globalcmt.org/CMTsearch.html).

Acknowledgments

References

Anderson, D. L. (1989). *Theory of the Earth*, Blackwell Scientific Publications, Boston, 366 pp.

Ando, M. (1979). The stress field of the Japan Islands in the last 0.5 million years, *Earth Mon. Symp.* **7,** 541–546.

Ando, M. (1984). *ScS* polarization anisotropy around the Pacific ocean, *J. Phys. Earth* **32,** 117–196.

Ando, M., Y. Ishikawa, and H. Wada (1980). *S*-wave anisotropy in the upper mantle under a volcanic area in Japan, *Nature* **286,** 43–46.

Backus, G. E. (1965). Possible forms of seismic anisotropy of the uppermost mantle under oceans, *J. Geophys. Res.* **70,** 3429–3439.

Bowman, J. R., and M. Ando (1987). Shear-wave splitting in the upper-mantle wedge above the Tonga subduction zone, *Geophys. J. R. Astr. Soc.* **88,** 25–41.

Chevrot, S., and N. Girardin (2000). On the detection and identification of converted and reflected phases from receiver functions, *Geophys. J. Int.* **141,** 801–808.

Crampin, S. (1970). The dispersion of surface waves in multilayered anisotropic media, *Geophys. J. R. Astr. Soc.* **21,** 387–402.

Crampin, S. (1978). Seismic wave propagation through a cracked solid: polarization as a possible dilatancy diagnostic, *Geophys. J. R. Astr. Soc.* **53,** 467–496.

Crampin, S. (1981). A view of wave motion in anisotropic and cracked elastic-medium, *Wave Motion* **3,** 343–391.

Frederiksen, A. W., and M. G. Bostock (2000). Modelling teleseismic waves in dipping anisotropic structures, *Geophys. J. Int.* **141,** 401–412.

Fryer, G. J., and L. N. Frazer (1984). Seismic wave in stratified anisotropic media, *Geophys. J. R. Astr. Soc.* **78,** 691–710.

Fukao, Y. (1984). Evidence from core-reflected shear waves for anisotropy in the Earth's mantle, *Nature* **309,** 695–698.

Girardin, N., and V. Farra (1998). Azimuthal anisotropy in the upper mantle from observations of *P*-to-*S* converted phases: application to southeast Australia, *Geophys. J. Int.* **133,** 615–629.

Haskell, N. A. (1962). Crustal reflection of plane *P* and *SV* waves, *J. Geophys. Res.* **67,** 4751–4767.

Hiramatsu, Y., M. Ando, T. Tsukuda, and T. Ooida (1998). Three-dimensional image of the anisotropic bodies beneath central Honshu, *Geophys. J. Int.* **135,** 801–816.

Hudson, J. A. (1981). Overall properties of a cracked solid, *Math. Proc. Cam. Phil. Soc.* **88,** 371–384.

Iidaka, T. (2003). Shear-wave splitting analysis of later phases in southwest Japan—a lineament structure detector inside the crust, *Earth Planets Space* **55,** 277–282.

Iidaka, T., and K. Obara (1995). Shear wave polarization anisotropy in the mantle wedge above the subducting Pacific plate, *Tectonophysics* **249,** 53–68.

Ishise, M., and H. Oda (2005). Three-dimensional structure of *P*-wave anisotropy beneath the Tohoku district, northeast Japan, *J. Geophys. Res.* **110,** B07304, doi 10.1029/2004JB003599.

Ishise, M., and H. Oda (2008). Subduction of the Philippine Sea slab in view of *P*-wave anisotropy, *Phys. Earth Planet. Interiors* **166,** 83–96.

Kamimoto, T. (2007). *P*-wave receiver functions of dipping boundary structure, *Graduation Thesis*, Okayama University, 1–38.

Kaneshima, S. (1990). Origin of crustal anisotropy: shear wave splitting studies in Japan, *J. Geophys. Res.* **95,** 11,121–11,133.

Kaneshima, S. (1991). Shear-wave splitting induced by seismic anisotropy in the earth, *J. Seism. Soc. Jpn.* **44,** 71–83.

Keith, C. M., and S. Crampin (1977a). Seismic body waves in anisotropic media: reflection and refraction at a plane interface, *Geophys. J. R. Astr. Soc.* **49,** 181–208.

Keith, C. M., and S. Crampin (1977b). Seismic body waves in anisotropic media: propagation through a layer, *Geophys. J. R. Astr. Soc.* **49,** 209–223.

Langston, C. A. (1979). Structure under Mount Rainer, Washington, inferred from teleseismic body waves, *J. Geophys. Res.* **84,** 4797–4762.

Levin, V., and J. Park (1997). *P-SH* conversion in a flat-layered medium with anisotropy of arbitrary orientation, *Geophys. J. Int.* **131,** 253–266.

Levin, V., and J. Park (1998). *P-SH* conversions in layered media with hexagonally symmetric anisotropy: a cookbook, *Pure Appl. Geophys.* **151,** 669–697.

Long, D. M., and R. B. van der Hilst (2005). Upper mantle anisotropy beneath Japan from shear wave splitting, *Phys. Earth Planet. Interiors* **151,** 206–222.

Long, D. M., and R. B. van der Hilst (2006). Shear wave splitting from local events beneath the Ryukyu arc: trench-parallel anisotropy in the mantle wedge, *Phys. Earth Planet. Interiors* **155,** 300–312.

Mainprice, D., and P. G. Silver (1993). Interpretation of *SKS*-waves using samples from the subcontinental lithosphere, *Phys. Earth Planet. Interiors* **78,** 257–280.

McNamara, D. E., and T. J. Owens (1993). Azimuthal shear wave velocity anomaly in the basin and range province using *Ps* converted phases, *J. Geophys. Res.* **98,** 12,003–12,017.

Montagner, J. P., and D. L. Anderson (1989). Petrological constraints on seismic anisotropy, *Phys. Earth Planet. Interiors* **54,** 82–105.

Nakamura, M., H. Watanabe, T. Konomi, S. Kimura, and K. Miura (1997). Characteristic activities of subcrustal earthquakes along the outer zone of southwestern Japan, *Ann. Disaster Prev. Res. Inst., Kyoto Univ.* **40,** 1–20.

Nakanishi, I. (1980). Precursors to *ScS* phases and dipping interface in the upper mantle beneath southwestern Japan, *Tectonophysics* **69,** 1–35.

Oda, H., and T. Douzen (2001). New evidence for a low-velocity layer on the subducting Phillipine Sea plate in southwest Japan, *Tectonophysics* **332,** 347–358.

Oda, H., and H. Shimizu (1997). *S* wave splitting observed in southwest Japan, *Tectonophysics* **270,** 73–82.

Owens, T. J., G. Zandt, and S. R. Taylor (1984). Seismic evidence for an ancient rift beneath the Cumberland Plateau, Tennessee: a detailed analysis of broadband teleseismic *P* waveforms, *J. Geophys. Res.* **89,** 7783–7795.

Park, J., and Y. Yu (1992). Anisotropy and coupled free oscillations: simplified models and surface waves observations, *Geophys. J. Int.* **110,** 401–420.

Peng, X., and E. D. Humphreys (1997). Moho dip and crustal anisotropy in northwestern Nevada from teleseismic receiver functions, *Bull. Seismol. Soc. Am.* **87,** 745–754.

Peng, X., and E. D. Humphreys (1998). Crustal velocity structure across the eastern Snake River Plain and the Yellowstone swell, *J. Geophys. Res.* **103,** 7171–7186.

Sacks, I. S., and J. A. Snoke (1977). The use of converted phases to infer the depth of the lithosphere-asthenosphere boundary beneath South America, *J. Geophys. Res.* **82,** 2011–2017.

Savage, M. K. (1998). Lower crustal anisotropy or dipping boundaries? Effects on receiver functions and a case study in New Zealand, *J. Geophys. Res.* **103,** 15,069–15,087.

Shibutani, T., M. Sambridge, and B. Kennett (1996). Genetic algorithm inversion for receiver functions with application to crust and uppermost mantle structure beneath eastern Australia, *Geophys. Res. Lett.* **23,** 1829–1832.

Silver, P. G., and W. W. Chang (1988). Implications of continental structure and evolution from seismic anisotropy, *Nature* **335,** 34–39.

Silver, P. G., and W. W. Chang (1991). Shear wave splitting and subcontinental mantle deformation, *J. Geophys. Res.* **96,** 16,429–16,454.

The Research Group of Active Faults of Japan (1991). *Active Faults in Japan*, Revised Ed., University of Tokyo Press, Tokyo, 1–437, sheet maps and inventories.

Tsukahara, H., and Y. Kobayashi (1991). Crustal stress in the central and western parts of Honshu, Japan, *J. Seism. Soc. Jpn.* **44,** 221–231.

Wessel, P., and W. H. F. Smith (1991). Free software helps map and display data, *Eos Trans. AGU* **72,** 441–446.

Yamauchi, M., K. Hirahara, and T. Shibutani (2003). High resolution receiver function imaging of the seismic velocity discontinuities in the crust and uppermost mantle beneath southwest Japan, *Earth Planets Space* **55,** 59–64.

Zhu, L. P., and H. Kanamori (2000). Moho depth variation in southern California from teleseismic receiver functions, *J. Geophys. Res.* **105,** 2969–2980.

Department of Earth Sciences
Okayama University
Okayama 700-8530, Japan
(M.N., H.O., H.A.)

Earthquake Research Institute
University of Tokyo
Tokyo 113-0032, Japan
(M.I.)